Convergent close-coupling calculations of electron scattering on math xmlns="http://www.w3.org/1998/Math/MathML">msup>mrow>mi>HeH/mi>/mrow>mo>+/mo>/msup>/math>

Liam H. Scarlett, Mark C. Zammit, Igor Bray, Barry I. Schneider, and Dmitry V. Fursa

Phys. Rev. A **106**, 042818 — Published 31 October 2022

DOI: 10.1103/PhysRevA.106.042818

Convergent close-coupling calculations of electron scattering on HeH^+

Liam H. Scarlett[1,2],* Mark C. Zammit[3], Igor Bray[2], Barry I. Schneider[4], and Dmitry V. Fursa[2]
[1] *Max-Planck-Institut für Plasmaphysik, Garching 85748, Germany*
[2] *Curtin Institute for Computation and Department of Physics and Astronomy, Curtin University, Perth, Western Australia 6102, Australia*
[3] *Theoretical Division, Los Alamos National Laboratory, Los Alamos, New Mexico 87545, USA and*
[4] *National Institute of Standards and Technology, Gaithersburg, Maryland 20899-8422, USA*
(Dated: October 11, 2022)

We use the molecular convergent close-coupling (MCCC) method to perform calculations of 10–1000 eV electron scattering on the ground state of HeH^+. Cross sections are presented for excitation of the $n = 2$–3 singlet and triplet states (where n is the united-atoms-limit principle quantum number), as well as ionization. We also present cross sections for He^+ and H^+ ion production following dissociative excitation and ionization. The He^+ production cross section is compared with the measurements of Lecointre, Jureta, Urbain, and Defrance [J. Phys. B At. Mol. Opt. Phys. **47**, 015203 (2014)]. We find that the MCCC results are up to 30% higher than experiment. This deserves further investigation to identify the source of the discrepancy. The results presented here can be downloaded from the MCCC database (mccc-db.org).

I. INTRODUCTION

The helium hydride molecular ion HeH^+ is comprised of the two most universally abundant elements, namely hydrogen and helium. While the neutral HeH molecule has a repulsive electronic ground state [1], the HeH^+ ion and its isotopologues have an electronic ground state and several excited states which support a number of bound vibrational levels [2]. Along with the hydrogen molecule, HeH^+ is expected to form in the cooler edge and divertor regions of fusion reactors [3], where it is well-known that electron collisions with molecular species play an important role in governing the plasma dynamics [4].

The HeH^+ molecule was the first molecule to form in the early stages of the universe [5], and is thought to be present in significant quantities in helium-rich stars, nebulae, and molecular clouds [6, 7]. Collisional reactions with the early-forming molecules such as HeH^+, H_2^+, H_2, LiH^+, and LiH would have had a significant effect on the gravitational collapse of interstellar clouds during the formation of the first stars [6].

Understanding the important influence of electron collisions with molecules in plasmas requires accurate cross-section data for many reactions over a broad range of collision energies. Previously, we have applied the molecular convergent close-coupling (MCCC) method [8] to studies of electron and positron scattering on H_2^+ and H_2 [9–14], and produced a comprehensive set of cross sections for vibrationally-resolved electronic excitation of H_2 and its isotopologues [15–17]. The accuracy and scope of the MCCC e^--H_2 collision data set has allowed it to be implemented in plasma models in fusion and astrophysical applications [18–20]. We now take the first step in the production of a similarly-accurate data set for the helium hydride ion, by applying the MCCC method to studies of electronic excitation and ionization from the ground (electronic and vibrational) state of HeH^+.

Previous calculations of electron scattering on HeH^+ have been predominantly focused on low incident energies. Early complex Kohn calculations by Orel et al. [21] studied dissociation of the molecule via electronic excitation of the repulsive $a\,^3\Sigma^+$ state in the 21–26 eV region, and subsequent work produced data for resonance-enhanced dissociation through the vibrational continuum of the ground electronic state [22, 23]. More recent Kohn calculations by Ertan et al. [24] revisited the dissociative excitation process, also including excitation of the $A\,^1\Sigma^+$ state and considering incident energies up to 40 eV. Numerous calculations have been performed of dissociative recombination of electrons with the HeH^+ ion [25, 26], as well as rotational and vibrational excitation below the first electronically-inelastic threshold [27–30].

Measurements for this collision complex are limited. Strömholm et al. [31] took measurements of dissociative recombination and dissociative excitation below 40 eV, while Lecointre et al. [32] measured cross sections for production of He^+ and He^{2+} fragments following dissociative excitation and ionization from threshold to 3000 eV. In both cases, the measurements do not differentiate between individual transitions, instead having contributions from a number of different dissociative processes.

In this paper, we present cross sections for electronic excitation of the first 18 excited electronic states of HeH^+, corresponding to those states which converge to the $n = 2$ and 3 states of Li^+ in the united-atoms limit, as well as ionization and an estimate of dissociative excitation for comparison with experiment. The electronic

* liam.scarlett@curtin.edu.au

TABLE I. List of HeH^+ states corresponding to the $n = 1$, 2, and 3 states of Li^+ in the united-atoms limit. States are ordered in terms of increasing energy at the equilibrium internuclear separation.

United atoms	Molecular state	Separated atoms
$n=1$		
$Li^+\left[^1S(1s^2)\right]$	$X\,^1\Sigma^+$	$He\left[^1S(1s^2)\right] + H^+$
$n=2$		
$Li^+\left[^3S(1s2s)\right]$	$a\,^3\Sigma^+$	$He^+(1s) + H(1s)$
$Li^+\left[^1S(1s2s)\right]$	$A\,^1\Sigma^+$	$He^+(1s) + H(1s)$
$Li^+\left[^3P(1s2p\pi)\right]$	$c\,^3\Pi$	$He\left[^3P(1s2p)\right] + H^+$
$Li^+\left[^3P(1s2p\sigma)\right]$	$b\,^3\Sigma^+$	$He\left[^3S(1s2s)\right] + H^+$
$Li^+\left[^1S(1s2p\pi)\right]$	$C\,^1\Pi$	$He^+(1s) + H(2\ell)$
$Li^+\left[^1P(1s2p\sigma)\right]$	$B\,^1\Sigma^+$	$He\left[^1S(1s2s)\right] + H^+$
$n=3$		
$Li^+\left[^3S(1s3s)\right]$	$d\,^3\Sigma^+$	$He\left[^3P(1s2p)\right] + H^+$
$Li^+\left[^1S(1s3s)\right]$	$D\,^1\Sigma^+$	$He^+(1s) + H(2\ell)$
$Li^+\left[^3P(1s3p\sigma)\right]$	$f\,^3\Sigma^+$	$He^+(1s) + H(2\ell)$
$Li^+\left[^1D(1s3d\sigma)\right]$	$E\,^1\Sigma^+$	$He^+(1s) + H(2\ell)$
$Li^+\left[^3P(1s3p\pi)\right]$	$e\,^3\Pi$	$He^+(1s) + H(2\ell)$
$Li^+\left[^1D(1s3d\pi)\right]$	$F\,^1\Pi$	$He\left[^1P(1s2p)\right] + H^+$
$Li^+\left[^3D(1s3d\delta)\right]$	$i\,^3\Delta$	$He\left[^3D(1s3d)\right] + H^+$
$Li^+\left[^1D(1s3d\delta)\right]$	$I\,^1\Delta$	$He\left[^1D(1s3d)\right] + H^+$
$Li^+\left[^3D(1s3d\pi)\right]$	$h\,^3\Pi$	$He\left[^3P(1s3p)\right] + H^+$
$Li^+\left[^3P(1s3p\pi)\right]$	$H\,^1\Pi$	$He\left[^1D(1s3d)\right] + H^+$
$Li^+\left[^3D(1s3d\sigma)\right]$	$g\,^3\Sigma^+$	$He^+(1s) + H(2\ell)$
$Li^+\left[^1P(1s3p\sigma)\right]$	$G\,^1\Sigma^+$	$He\left[^1P(1s2p)\right] + H^+$

states considered in the present work are listed in Table I, along with their corresponding united-atoms Li^+ states and separated-atoms dissociation fragments. The Latin letters prepended to the molecular state labels cannot be uniquely assigned based on energy ordering since there are a number of states whose potential-energy curves cross. We have adopted the HeH^+ state labels as defined by Michels [33], who assigned them based on energy ordering in the separated-atoms limit. The states we have labeled $i\,^3\Delta$, $I\,^1\Delta$, $h\,^3\Pi$, and $H\,^1\Pi$ were not studied by Michels [33], however we have assigned these labels based on the same rule. In Fig. 1 we show the potential-energy curves of the HeH^+ states under consideration in the present work, as well as the ground state of the HeH^{2+} ion. Although some of the excited electronic states have minima in their potential-energy curves, they are well outside the Franck-Condon region of the $X\,^1\Sigma^+(v=0)$ state. Therefore all excitations, as well as ionization, from the ground electronic and vibrational state can be considered dissociative. Whenever the effects of nuclear motion are discussed in the present work we refer only to the $^4HeH^+$ isotopologue; the effects of isotopic substitution can be explored in future work.

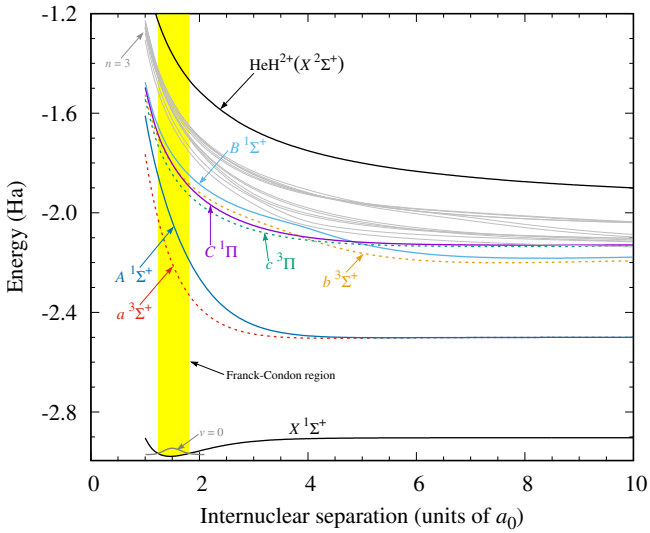

FIG. 1. Potential-energy curves of the $n = 1$–3 electronic states of HeH^+, taken from Loreau et al. [2], and the HeH^{2+} ground state, taken from Jungen and Jungen [34]. Also shown is the $v=0$ vibrational wave function in the ground electronic state of HeH^+, and its associated Franck-Condon region.

II. THEORY

The MCCC method has been developed in both the spherical and prolate-spheroidal coordinate systems, each with different strengths depending on the range of internuclear separations which are relevant to the calculations. In the present work, where we are concerned only with scattering on the ground vibrational level, we have found that a spherical coordinate system with the origin centered on the helium atom is the most appropriate. The spherical MCCC method and its application to H_2 have been discussed in detail in previous publications [8, 12]. Here, only a brief overview is given, with particular focus on those aspects which are different for scattering on heteronuclear diatomics such as HeH^+. Atomic units are used throughout, unless specified otherwise.

A. Molecular structure

The target is represented in a body-fixed spherical coordinate system, with the z axis aligned with the internuclear axis. In previous MCCC calculations for H_2^+ and H_2, the origin was placed at the geometric center of the nuclei [8], however for heteronuclear molecules it is beneficial to allow the flexibility of placing the origin at any point along the z axis between the two nuclei. This is

illustrated in Fig. 2.

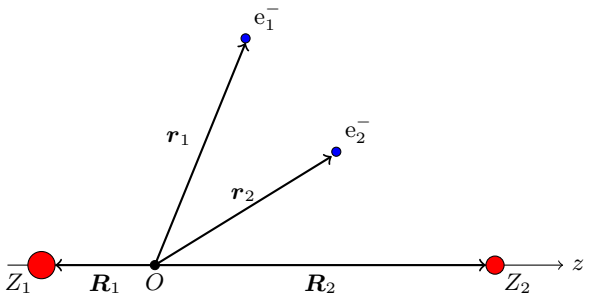

FIG. 2. Representation of a two-electron heteronuclear diatomic molecule in a spherical coordinate system with the origin positioned at an arbitrary point between the two nuclei.

We represent the molecular wave functions within the Born-Oppenheimer approximation, and neglect the rotational motion, defining the vibronic (vibrational and electronic) wave function by

$$\Phi_{nv}(\boldsymbol{r}_1, \boldsymbol{r}_2, R) = \Phi_n(\boldsymbol{r}_1, \boldsymbol{r}_2; R)\nu_{nv}(R), \tag{1}$$

where $\boldsymbol{r}_1$ and $\boldsymbol{r}_2$ are the electronic coordinates, $R = R_1 + R_2$ is the internuclear separation, Φ_n is an electronic wave function (with R treated as a parameter), ν_{nv} is a vibrational wave function, n indexes the electronic states, and v is the vibrational quantum number. The electronic states are eigenstates of the electronic Hamiltonian

$$\hat{H}_{12} = \hat{K}_1 + \hat{V}_1 + \hat{K}_2 + V_2 + V_{12} + \frac{1}{R}. \tag{2}$$

Here, $\hat{K}_i$ is the one-electron kinetic-energy operator, V_i is the electron-nuclei potential, and V_{12} is the electron-electron potential:

$$\hat{K}_i = -\frac{1}{2}\nabla_i^2 \tag{3}$$

$$V_i = \frac{z_i Z_1}{|\boldsymbol{r}_i - \boldsymbol{R}_1|} + \frac{z_i Z_2}{|\boldsymbol{r}_i - \boldsymbol{R}_2|} \tag{4}$$

$$V_{ij} = \frac{z_i z_j}{|\boldsymbol{r}_i - \boldsymbol{r}_j|}. \tag{5}$$

The potentials are expanded in spherical harmonics:

$$V_i(\boldsymbol{r}_i) = z_i \sum_{\lambda=0}^{\infty} \sqrt{\frac{4\pi}{2\lambda+1}} Y_\lambda^0(\hat{\boldsymbol{r}}_i) \times \left[Z_1 v_\lambda(r_i, R_1) + (-1)^\lambda Z_2 v_\lambda(r_i, R_2)\right] \tag{6}$$

$$V_{ij}(\boldsymbol{r}_i, \boldsymbol{r}_j) = z_i z_j \sum_{\lambda=0}^{\infty} \sum_{\mu=-\lambda}^{\lambda} \frac{4\pi}{2\lambda+1} v_\lambda(r_i, r_j) Y_\lambda^{-\mu}(\hat{\boldsymbol{r}}_i) Y_\lambda^{\mu}(\hat{\boldsymbol{r}}_j), \tag{7}$$

where

$$v_\lambda(r_i, r_j) = \frac{[\min(r_i, r_j)]^\lambda}{[\max(r_i, r_j)]^{\lambda+1}}. \tag{8}$$

At each fixed value of R, the target space is represented by a set of pseudostates obtained from a configuration-interaction (CI) calculation using Sturmian basis functions. In the spherical-coordinate MCCC method we utilize the following basis for the one-electron coordinate and spin space:

$$\langle \boldsymbol{r}|k\ell m\sigma\rangle = \frac{1}{r}\varphi_{k\ell}(r) Y_\ell^m(\hat{\boldsymbol{r}})\chi(\sigma), \qquad k = 1, 2, \ldots \tag{9}$$

where $\chi(\sigma)$ is the one-electron spin wave function for spin projection σ, Y_ℓ^m are the spherical Harmonics, and $\varphi_{k\ell}$ are the following radial Laguerre basis functions:

$$\varphi_{k\ell}(r) = \sqrt{\frac{\alpha_\ell (k-1)!}{(k+\ell)(k+2\ell)!}} (2\alpha_\ell r)^{\ell+1} e^{-\alpha_\ell r} L_{k-1}^{2\ell+1}(2\alpha_\ell r). \tag{10}$$

Here, $L_{k-1}^{2\ell+1}$ are the associated Laguerre polynomials, and α_ℓ are tunable exponential falloff parameters.

For each target symmetry (m, s) we construct a set of antisymmetrized two-electron configurations:

$$|k_1\ell_1 m_1 k_2\ell_2 m_2 : ms\rangle = \frac{1}{\sqrt{2(1+\delta_{k_1 k_2}\delta_{\ell_1\ell_2}\delta_{m_1 m_2})}} \times \sum_{\sigma_1\sigma_2} C^{sm_s}_{\frac{1}{2}\sigma_1, \frac{1}{2}\sigma_2} \mathcal{A}|k_1\ell_1 m_1\sigma_1\rangle|k_2\ell_2 m_2\sigma_2\rangle, \tag{11}$$

where $\mathcal{A}$ is the antisymmetrization operator, $C^{sm_s}_{s_1\sigma_1, s_2\sigma_2}$ are the Clebsch-Gordan coefficients, and we require that $m_1 + m_2 = m$ due to axial symmetry. The two-electron pseudostates obtained from the CI calculation are given by

$$|\Phi_n : ms\rangle = \sum_\gamma C_\gamma^{(n)} |\gamma : ms\rangle, \tag{12}$$

and satisfy

$$\langle ms : \Phi_{n'}|\hat{H}_{12}|\Phi_n : ms\rangle = \epsilon_n \delta_{n'n}, \tag{13}$$

where $\gamma = (k_1\ell_1 m_1 k_2\ell_2 m_2)$, $C_\gamma^{(n)}$ are the CI coefficients, and ϵ_n is the pseudostate energy.

B. Projectile wave functions

For scattering on an ionic target the projectile is asymptotically described by a Coulomb wave function. Additionally, a short-ranged distorting potential U_0 can be incorporated into the scattering calculations for reasons of numerical stability and computational performance. Hence we define projectile distorted waves $|\boldsymbol{k}^{(\pm)}\rangle$ with energy ϵ_k by

$$(\epsilon_k^{(\pm)} - \hat{K}_0 - z_0 Z_{\rm asym}/r_0 - U_0)|\boldsymbol{k}^{(\pm)}\rangle = 0, \tag{14}$$

where $Z_{\rm asym}$ is the asymptotic target charge ($Z_{\rm asym} = +1$ for HeH^+). The distorted waves are expanded in partial

waves:

$$|\boldsymbol{k}^{(\pm)}\rangle = \frac{1}{k}\sum_{L=0}^{\infty}\sum_{M=-L}^{L} i^L e^{\pm i(\sigma_L+\delta_L)}|kLM\rangle Y_L^{M*}(\hat{\boldsymbol{k}}), \quad (15)$$

where σ_L and δ_L are the Coulomb and distorting phase shifts, respectively.

The asymptotic Coulomb potential supports an infinite number of bound projectile states, while the distorting potential supports a finite number of bound states. We combine these two potentials and define the one-dimensional projectile Hamiltonian:

$$\hat{H}_0 = -\frac{1}{2}\frac{\mathrm{d}^2}{\mathrm{d}r_0^2} + \frac{L(L+1)}{2r_0^2} + \frac{z_0 Z_{\rm asym}}{r_0} + U_0(r_0), \quad (16)$$

which we diagonalize in the single-particle Laguerre basis given in Eq. (9) to obtain bound projectile states for each angular momentum L. After suitable normalization these states can then be included in the scattering equations in addition to the distorted continuum waves $|kLM\rangle$.

C. Scattering equations

Following Ref. [8], we solve the Schrödinger equation with outgoing spherical-wave boundary conditions (indicated by the (+) superscript):

$$(E^{(+)} - \hat{H}_{\rm asym})|\psi_i^{\mathcal{S}(+)}\rangle = \hat{V}_U|\psi_i^{\mathcal{S}(+)}\rangle, \quad (17)$$

where E, $\mathcal{S}$, and ψ are respectively the total scattering-system energy, spin, and wave function for initial target state i,

$$\hat{H}_{\rm asym} = \hat{H}_{12} + \hat{K}_0 + \frac{z_0 Z_{\rm asym}}{r_0} + U_0 \quad (18)$$

is the asymptotic Hamiltonian, and the interaction potential is

$$\hat{V}_U = V_0 + V_{01} + V_{02} - \frac{z_0 Z_{\rm asym}}{r_0} - U_0 + (E - \hat{H})\sum_{j=1}^{2}\hat{P}_{0j}. \quad (19)$$

The final term in V_U is the exchange potential operator (P_{0j} is the electron permutation operator), which appears as a result of enforcing the antisymmetry of the total scattering wave function.

Following standard procedure in the MCCC method [8], the total scattering wave function is expanded in the basis formed by the target electronic states. After substituting this expansion into Eq. (17) and applying the projectile partial-wave expansion (15) we obtain the partial-wave Lippmann-Schwinger equation:

$$T^{\mathcal{MS}}_{fL_fM_f,iL_iM_i}(k_f,k_i) = V^{\mathcal{MS}}_{fL_fM_f,iL_iM_i}(k_f,k_i) + \sum_{nLM}\!\!\!\!\!\!\int \mathrm{d}k \frac{V^{\mathcal{MS}}_{fL_fM_f,nLM}(k_f,k)T^{\mathcal{MS}}_{nLM,iL_iM_i}(k,k_i)}{E^{(+)}-\epsilon_k-\epsilon_n}, \quad (20)$$

where the partial-wave V-matrix elements are defined by

$$V^{\mathcal{MS}}_{fL_fM_f,iL_iM_i}(k_f,k_i) \equiv \langle \mathcal{MS}: k_f L_f M_f \Phi_f|\hat{V}_U|\Phi_i k_i L_i M_i: \mathcal{MS}\rangle. \quad (21)$$

Eq. (20) is solved per total scattering-system angular-momentum projection $\mathcal{M}$ and spin $\mathcal{S}$, using techniques described in Ref. [8]. The sum/integral over k indicates the presence of bound projectile states, which are included in the calculations until convergence is reached. Once the distorted-wave partial T-matrix elements are computed, the physical matrix elements are obtained using [35]

$$T^{\mathcal{MS}}_{fL_fM_f,iL_iM_i}(q_f,q_i) = T^{\mathcal{MS}}_{fL_fM_f,iL_iM_i}(k_f,k_i)e^{i(\delta_{L_i}+\delta_{L_f})} - \delta_{f,i}\delta_{L_f,L_i}\delta_{M_f,M_i}\frac{q_i}{\pi}e^{i\delta_{L_i}}\sin(\delta_{L_i}), \quad (22)$$

where q is used to indicate projectile waves calculated without the presence of the distorting potential (Coulomb waves in the present case). When solving Eq. (20), we check for convergence with respect to the number of target states and maximum projectile partial-wave angular momentum $L_{\rm max}$. We perform calculations for all $|\mathcal{M}| \le L_{\rm max}$.

D. Distorting potential

The short-ranged distorting potential U_0 is chosen to cancel the spherical part of the V_0, V_{01}, and V_{02} potentials, and is given in Ref. [8] for the case where the spherical coordinate-system origin is placed at the geometric center of the nuclei. For the more general case with the origin placed at an arbitrary point along the internuclear axis, it is given by

$$U_0(r_0) = z_0 Z_1 v_0(r_0,R_1) + z_0 Z_2 v_0(r_0,R_2) - \frac{z_0 Z_{\rm asym}}{r_0} - 2z_0\iint |\Phi_1(\boldsymbol{r}_1,\boldsymbol{r}_2)|^2 v_0(r_0,r_1)\,\mathrm{d}\boldsymbol{r}_1\mathrm{d}\boldsymbol{r}_2, \quad (23)$$

where Φ_1 is the target ground-state wave function.

E. Fixed-nuclei cross sections and Born completion

At each fixed internuclear separation R, we define the partial-wave scattering amplitudes:

$$F^{\mathcal{MS}}_{fL_fM_f,iL_iM_i}(R) = \frac{-4\pi^2}{q_f q_i} i^{L_i-L_f}e^{i(\sigma_{L_i}+\sigma_{L_f})} \times T^{\mathcal{MS}}_{fL_fM_f,iL_iM_i}(q_f,q_i;R), \quad (24)$$

which are used to calculate the partial-wave integrated cross sections (ICS)

$$\sigma^{\mathcal{MS}}_{f,i}(R) = \frac{1}{4\pi}\frac{q_f}{q_i}\sum_{L_fM_f}\sum_{L_iM_i}\left|F^{\mathcal{MS}}_{fL_fM_f,iL_iM_i}(R)\right|^2, \quad (25)$$

and, in turn, the spin-resolved ICS

$$\sigma^{\mathcal{S}}_{f,i}(R) = \sum_{\mathcal{M}} \sigma^{\mathcal{M}\mathcal{S}}_{f,i}(R). \tag{26}$$

For scattering on the ground state of HeH^+ (spin zero), only $\mathcal{S} = \frac{1}{2}$ is possible, so from here on we drop the dependence on $\mathcal{S}$.

When performing calculations for neutral targets we accelerate the convergence with respect to $L_{\max}$ by a straight-forward application of the analytic Born completion technique, which is described in Ref. [14]. This technique assumes that for higher partial waves the partial cross sections converge to the plane-wave Born partial cross sections, however for scattering on ionic targets they converge to the Coulomb-wave Born partial cross sections. Hence, we adopt the following approach. First, T-matrix elements are obtained from the close-coupling calculation for partial waves up to $L_{\max}$. These are then supplemented by partial-wave (Coulomb) V-matrix elements up to a much larger $\bar{L}$ (in the present work we have found $\bar{L} = 40$ to be more than sufficient). Finally, the standard plane-wave Born completion technique is applied to account for partial waves above $\bar{L}$.

F. Adiabatic-nuclei cross sections

We apply the adiabatic-nuclei (AN) approximation, and since we are not concerned with the fully vibrationally-resolved processes at present, we utilize the completeness of the vibrational spectrum to calculate the total electronic excitation cross sections (summed over final rovibrational states):

$$\sigma_{f,iv_i} = \langle \nu_{iv_i} | \sigma_{f,i}(R) | \nu_{iv_i} \rangle, \tag{27}$$

where the bra-kets imply integration over the internuclear separation R. The vibrational wave functions $\nu_{iv_i}(R)$ are obtained from a diagonalization procedure similar to what is used in the electronic structure calculations. More specific details of the vibrational structure calculation and AN approximation can be found in Ref. [14]. At energies sufficiently far away from the excitation threshold, Eq. (27) can be well approximated by the fixed-nuclei (FN) cross section evaluated at the mean internuclear separation of the ground vibrational wave function. In the present work, we utilize both the FN and AN approximations, with the latter applied at near-threshold energies where the FN approximation breaks down. This will be discussed further in Sec. IV.

III. CALCULATION DETAILS

A. Target structure

It is necessary to find a balance between target-structure accuracy and tractability of the scattering calculations, since increasing the size of the basis for the CI calculation leads to more pseudostates which must be included in the close-coupling expansion. As in previous work [12, 14, 36], we adopt a hybrid-basis approach which is optimized to yield sufficiently accurate low-lying target states without the computational expense of the scattering calculations becoming prohibitive. The main set of basis orbitals is comprised of Laguerre functions (9) with $k \leq N_\ell$ and exponential falloffs $\alpha_\ell = 1.4$ for each $\ell \leq \ell_{\max}$. A number of models with different N_ℓ and $\ell_{\max}$ will be utilized in the convergence studies discussed later. The $1s$ and $2p$ Laguerre functions are replaced by an accurate HeH^{2+} ground state ($1s\sigma$) and first excited state ($2p\sigma$) obtained from a preliminary one-electron diagonalization with $N_\ell = 15 - \ell$, $\ell_{\max} = 8$, and $\alpha_\ell = 5.0$. The $2s$, $3p$, and $3d$ orbitals are then replaced with Laguerre functions with exponential falloffs

$$\alpha_\ell = \begin{cases} 2.22, & \ell = 0 \\ 1.92, & \ell = 1 \\ 2.58, & \ell = 2 \end{cases}, \tag{28}$$

which are chosen to optimize the low-lying target-state energies. To reduce computational expense, we use a restricted CI calculation with the set of two-electron configurations (11) consisting of all "frozen-core" configurations $(1s, n\ell)$, and correlation configurations $(n\ell, n'\ell')$ with both electrons allowed to occupy the $1s$, $2s$, $2p$, $3p$, and $3d$ orbitals.

The equilibrium separation of the $X\,^1\Sigma^+$-state potential-energy curve is at $R = 1.463$ [37], and we have calculated the mean separation of the $v = 0$ vibrational wave function to be $R = 1.518$. In Fig. 3 we show the HeH^+ ground-state potential-energy curve calculated by Loreau et al. [2], along with our calculated vibrational wave function. The equilibrium and mean internuclear separations are indicated on the figure.

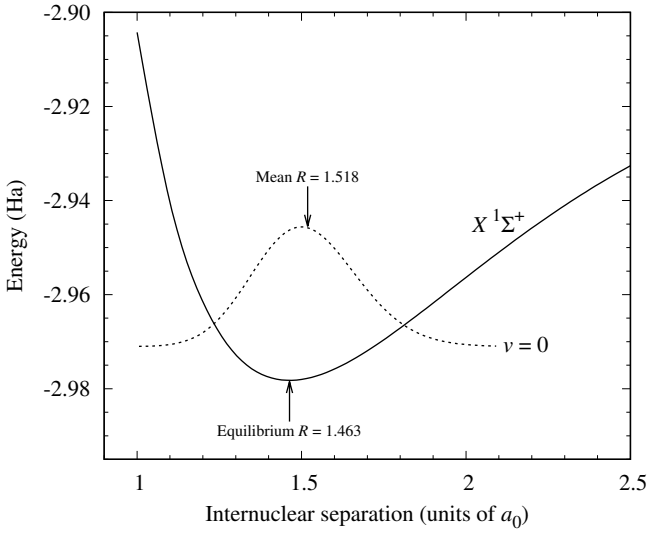

FIG. 3. Potential-energy curve of the HeH^+ $X\,^1\Sigma^+$ state calculated by Loreau et al. [2], and the $v = 0$ vibrational wave function.

TABLE II. Two-electron energies and vertical excitation energies for the $n=1$–3 states of HeH^+ calculated at an internuclear separation of $R=1.5$ a_0. Comparison is made between the MCCC energies and the accurate calculations of Jungen and Jungen [34]. In the final row the same is shown for the ground state of HeH^{2+}.

	Energy (Ha)		ΔE (eV)		
State	MCCC	Ref. [34]	MCCC	Ref. [34]	Error
		$n=1$			
$X\,^1\Sigma^+$	−2.9677	−2.9780	—	—	—
		$n=2$			
$a\,^3\Sigma^+$	−2.1905	−2.2036	21.056	21.072	−0.016 (0.08%)
$A\,^1\Sigma^+$	−2.0248	−2.0357	25.673	25.641	0.032 (0.12%)
$c\,^3\Pi$	−1.8408	−1.8451	30.739	30.827	−0.088 (0.29%)
$b\,^3\Sigma^+$	−1.8014	−1.8056	31.844	31.901	−0.057 (0.18%)
$C\,^1\Pi$	−1.8000	−1.8042	31.874	31.940	−0.066 (0.21%)
$B\,^1\Sigma^+$	−1.7616	−1.7652	32.916	33.000	−0.084 (0.25%)
		$n=3$			
$d\,^3\Sigma^+$	−1.6476	−1.6501	36.078	36.132	−0.054 (0.15%)
$D\,^1\Sigma^+$	−1.6226	−1.6254	36.775	36.806	−0.031 (0.08%)
$f\,^3\Sigma^+$	−1.5918	−1.5954	37.636	37.621	0.015 (0.04%)
$E\,^1\Sigma^+$	−1.5901	−1.5929	37.682	37.690	−0.008 (0.02%)
$e\,^3\Pi$	−1.5901	−1.5904	37.686	37.757	−0.071 (0.19%)
$F\,^1\Pi$	−1.5873	−1.5881	37.751	37.819	−0.068 (0.18%)
$i\,^3\Delta$	−1.5791	−1.5788	37.998	38.073	−0.075 (0.20%)
$I\,^1\Delta$	−1.5788	−1.5784	38.009	38.083	−0.074 (0.19%)
$h\,^3\Pi$	−1.5809	−1.5781	38.059	38.091	−0.032 (0.08%)
$H\,^1\Pi$	−1.5737	−1.5672	38.398	38.389	0.009 (0.02%)
$g\,^3\Sigma^+$	−1.5742	−1.5650	38.460	38.448	0.012 (0.03%)
$G\,^1\Sigma^+$	−1.5681	−1.5534	38.846	38.765	0.081 (0.21%)
HeH^{2+}	−1.3606	−1.3621	43.731	43.971	−0.240 (0.55%)

In the convergence studies discussed later in Sec. III B we use a target basis with $\ell_{\max}=4$ and $N_\ell=N_{\max}-\ell$, with $N_{\max}=10$, 12, and 14. The energies for the $n=1$–3 states in the $N_{\max}=12$ and 14 models are in agreement up to the third decimal place (in Hartrees). The absolute energies and excitation energies calculated at $R=1.5$ are presented in Table II and compared with accurate calculations from Jungen and Jungen [34]. The agreement is very good, with the errors in the excitation energies all being less than 0.1 eV (less than 0.3%). The static dipole polarizability of the ground state, and dipole moments for a selection of transitions are presented in Table III and compared with available results from the literature. The present dipole moments compare favorably with the accurate calculations with all errors being less than 5% and several less than 1%. Compared to our previous calculations of electron scattering on H_2 [12], this level of accuracy in the target structure is very good, and when it comes to estimating the uncertainty in the calculated cross sections later we expect that the small errors here will be negligible compared to the uncertainty due to the level of convergence in the scattering calculations, and hence can be neglected.

TABLE III. Static dipole polarizability of the HeH^+ $X\,^1\Sigma^+$ state, and dipole moments for a selection of electronic transitions. Comparison is made between the present MCCC structure calculation and the accurate calculations of Michels [33] and Bishop and Cheung [38]. The internuclear separation R at which each quantity is calculated varies depending on the data available in Refs. [33, 38], and is indicated in the table.

Quantity	R	MCCC	Ref.	Error
Parallel polarizability	1.46	1.542	1.542[a]	0.0%
Perpendicular polarizability	1.46	0.857	0.851[a]	0.6%
Total polarizability	1.46	1.086	1.081[a]	0.5%
$X\,^1\Sigma^+ \to A\,^1\Sigma^+$ dipole moment	1.5	0.810	0.798[b]	1.2%
$X\,^1\Sigma^+ \to C\,^1\Pi$ dipole moment	1.5	0.576	0.579[b]	0.3%
$X\,^1\Sigma^+ \to A\,^1\Sigma^+$ dipole moment	2.0	0.856	0.870[b]	1.4%
$X\,^1\Sigma^+ \to C\,^1\Pi$ dipole moment	2.0	0.597	0.586[b]	1.1%
$A\,^1\Sigma^+ \to C\,^1\Pi$ dipole moment	2.0	0.415	0.384[b]	3.1%
$a\,^3\Sigma^+ \to c\,^3\Pi$ dipole moment	2.0	0.546	0.589[b]	4.3%

[a]Bishop and Cheung [38]
[b]Michels [33]

B. Scattering models and target-state convergence

We first verify convergence with respect to the number of target states included in the calculations, while keeping the partial-wave expansion fixed with $L_{\max}=6$. In Table IV we describe a number of models with increasing numbers of target states. The models are labeled in the format MCC(N) or MCCC(N), where N is the number of states (counting degeneracy), and the MCC label indicates that only bound states are included while MCCC indicates that continuum pseudostates are also present to model coupling to ionization channels. To ensure convergence in both the discrete and ionization cross sections, we include all states generated from the structure calculation in the close-coupling expansion, with two exceptions. Firstly, states with orbital angular-momentum projection $m > 3$ are not included in any of the models. Secondly, we exclude all states with a $1s$ core-orbital spectroscopic factor less than 0.1. The definition of the spectroscopic factor and further discussion of the procedure for removing states based on this quantity is given in Ref. [39]. We have verified that all states we exclude make an insignificant contribution to the ionization cross section in the Born approximation and hence it is reasonable to exclude them from the close-coupling calculations. Although excluding states from the close-coupling expansion significantly reduces the use of computational resources, it comes at the cost of not being able to resolve the problem of non-uniqueness in the scattering

TABLE IV. Description of the various target models used in the present MCCC calculations. The number in parentheses after the MCC/MCCC labels indicates the number of target states, counting degeneracy. The united-atoms principle quantum number is denoted by n, while m refers to the orbital angular-momentum projection, and S refers to the spectroscopic factor discussed in the text.

Model	Laguerre basis	States included
MCC(9)	$N_\ell = 10-\ell,\ \ell \le 4$	All $n=1$–2 states
MCC(27)	$N_\ell = 10-\ell,\ \ell \le 4$	All $n=1$–3 states
MCC(98)	$N_\ell = 10-\ell,\ \ell \le 4$	All bound $m \le 3$ states
MCCC(357)	$N_\ell = 10-\ell,\ \ell \le 4$	All $m \le 3$ states with $S \ge 0.1$
MCCC(448)	$N_\ell = 12-\ell,\ \ell \le 4$	All $m \le 3$ states with $S \ge 0.1$
MCCC(546)	$N_\ell = 14-\ell,\ \ell \le 4$	All $m \le 3$ states with $S \ge 0.1$

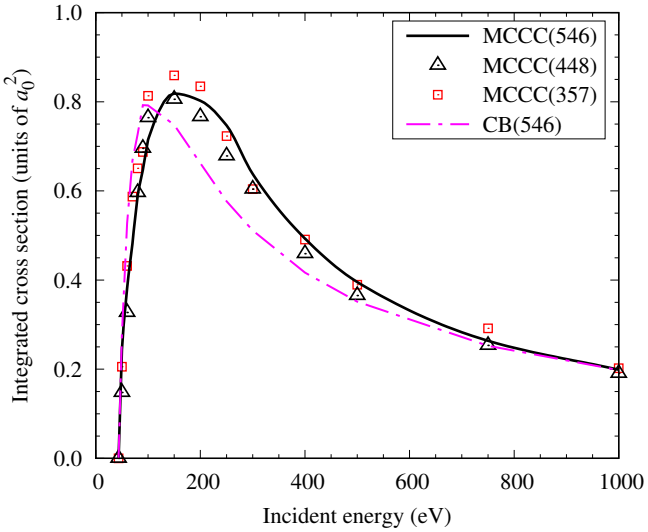

FIG. 4. Convergence studies, for ionization of the $X\,^1\Sigma^+$ of HeH^+ at $R=1.518\ a_0$. Convergence is tested with respect to the number of target states included in the close-coupling expansion. See the text for a description of the different scattering models. CB(546) refers to the Coulomb-Born approximation applied using the same continuum pseudostates present in the MCCC(546) model.

calculations. This issue, which has been discussed previously [8], can lead to some numerical instability in the calculated cross sections, and at present our only solution is an algebraic technique which requires the inclusion of all pseudostates generated from the Laguerre basis (for two-electron targets). We have found previously that the instabilities in the integrated cross sections are generally minor and predominantly affect transitions with small cross sections. The particular non-unique off-shell solution one obtains when solving Eq. (20) numerically is determined by the choice of Gaussian quadrature knots used to represent the integral over k. A given integration mesh will generally lead to unstable results at a few different incident energies, and hence it is straightforward to repeat those affected calculations with a different choice of knots in order to force a different off-shell solution and obtain cross sections which are smooth functions of energy.

The convergence studies have been performed at the mean internuclear separation of $R = 1.518$. Fig. 4 compares the ionization cross section calculated with the MCCC(357), MCCC(448), and MCCC(546) models (the three which include continuum pseudostates), along with the Coulomb-Born approximation applied using the MCCC(546) pseudostates. The cross section is sufficiently converged over the entire energy range with the MCCC(546) model, and the limit in which the Coulomb-Born approximation is valid is reached at around 1000 eV. Although it is normally expected that Born or Coulomb-Born cross sections should be larger than the result of close-coupling, the present Coulomb-Born ionization cross section is smaller than the MCCC calculation for energies around 150 eV and above. The reason for this is that the contribution to the ionization cross section from exchange transitions (which are not accounted for in the Coulomb-Born calculation) is sufficiently large for this target as to exceed the difference between Coulomb-Born and MCCC for the direct transitions. Hence, the total MCCC ionization cross section can become larger than the Coulomb-Born cross section. This point is illustrated in Fig. 5, where the MCCC(546) ionization cross section is decomposed into contributions from excitation of singlet and triplet pseudostates, for internuclear separations $R=0$ and 1.518. For $R=0$ we compare with CCC calculations for ionization of atomic Li^+ [40], which is the united-atoms limit of HeH^+, to verify the validity of the MCCC calculations. In the atomic case, the exchange contribution reaches a peak at twice the ionization threshold and then decays and becomes negligible by 10 times the ionization threshold. However, in the molecular case the decay is slower, and exchange effects must still be accounted for at energies up to 20 times the ionization threshold (approximately 1000 eV). The reason for the flatter peak in the exchange contribution at $R = 1.518$ is that higher-energy triplet pseudostates with excitation energies up to 4 times the ionization threshold are still important, which is not the case at $R=0$. Since the HeH^+ electrons are less tightly bound than the Li^+ electrons, it is expected that the exchange interaction will be more important.

In Fig. 6 we present convergence studies for excitation of the $n = 2$ states ($a\,^3\Sigma^+$, $A\,^1\Sigma^+$, $c\,^3\Pi$, $b\,^3\Sigma^+$, $C\,^1\Pi$, and $B\,^1\Sigma^+$). Since the excitation cross sections for a charged target are generally non-zero at threshold, the threshold energies for all FN calculations presented in this paper are indicated by vertical lines on the figures. The MCC(9) and MCC(27) models have been run on a finer energy grid to show the presence of a large number of resonances below the ionization threshold (≈ 44 eV), as well as pseudoresonances at higher energies. A more detailed view of the resonance structures in the MCC(27)

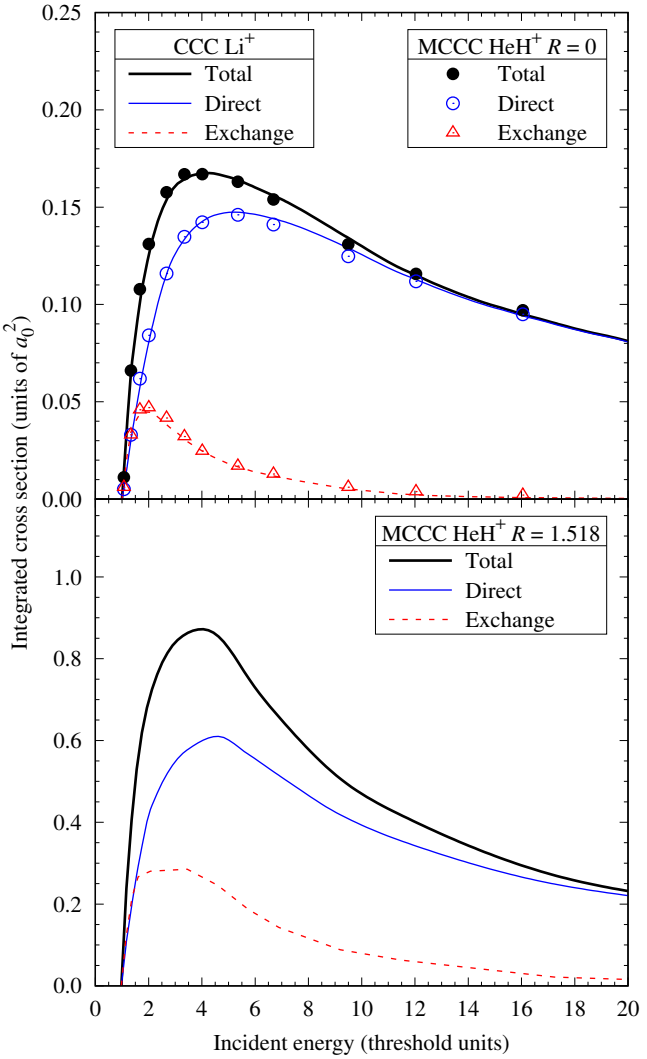

FIG. 5. Electron-impact ionization cross section for HeH^+, comparing the contribution from direct and exchange transitions (excitation of singlet and triplet pseudostates, respectively). In the top panel, the MCCC(546) model is run at zero internuclear separation and compared with the CCC calculations for electron scattering on atomic Li^+ [40]. In the bottom panel, the MCCC(546) model is run at the HeH^+ mean internuclear separation of $R = 1.518$ a_0. The cross sections are presented as a function of the incident energy in threshold units (the ionization threshold is 74.8 eV for $R = 0$ and 43.5 eV for $R = 1.518$ a_0).

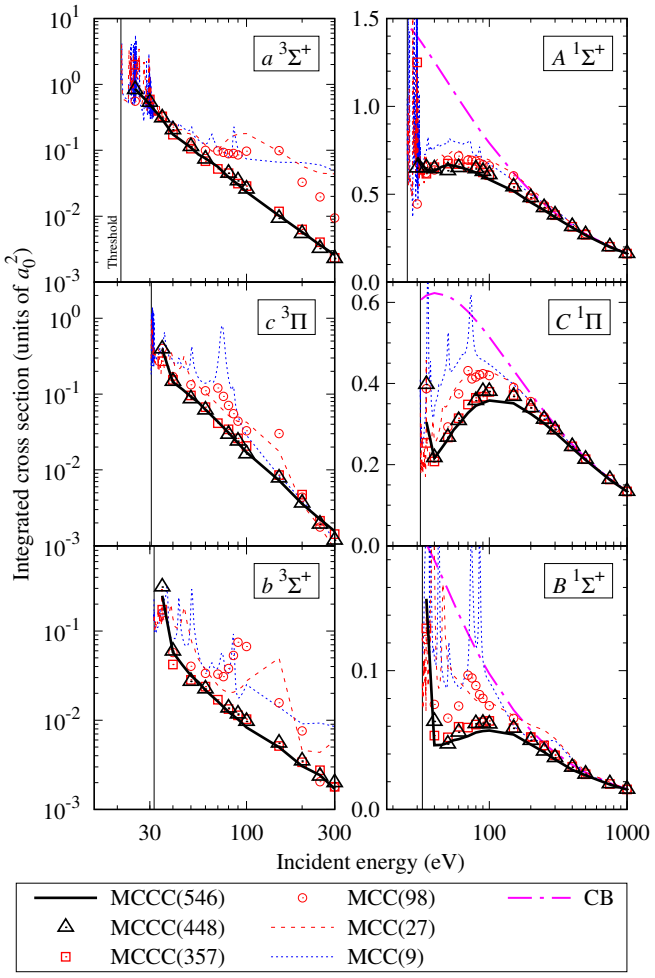

FIG. 6. Convergence studies for excitation of the $n = 2$ electronic states from the $X\,^1\Sigma^+$ state of HeH^+ at $R = 1.518$ a_0. Convergence is tested with respect to the number of target states included in the close-coupling expansion. The Coulomb-Born (CB) cross sections are also shown for the singlet states. See the text for a description of the different scattering models.

$X\,^1\Sigma^+ \rightarrow a\,^3\Sigma^+$ cross section is given in Fig. 7. To allow comparison with the FN complex Kohn calculations of Orel et al. [21], the cross section presented in Fig. 7 is calculated at the equilibrium internuclear separation ($R = 1.455$) rather than the mean. We have indicated three features in the figure that are present in both the MCC(27) and Kohn cross sections. Feature number one is not a resonance, but simply the sharp rise in the cross section at threshold characteristic of exchange transitions, followed by a rapid decay. The location of this feature differs by about 0.4 eV between the two calculations since the target wave functions in the present calculations are slightly more accurate (the key difference is likely a lower ground-state energy in the MCCC structure model leading to higher excitation energies compared to Ref. [21]). Feature number three was identified in Ref. [21] as a Feschbach resonance, and it is reproduced in the present calculations, also at a slightly higher energy. The remaining resonances above 24 eV are all Feschbach resonances, and aside from some which are missing in the Kohn calculations due to insufficient energy resolution, the two calculations appear to predict the same structures in the cross section (once the shift in energy is taken into account). Feature number two was identified in Ref. [21] as a shape resonance, and we find that there is essentially perfect agreement between the two calculations here. It is unclear why the

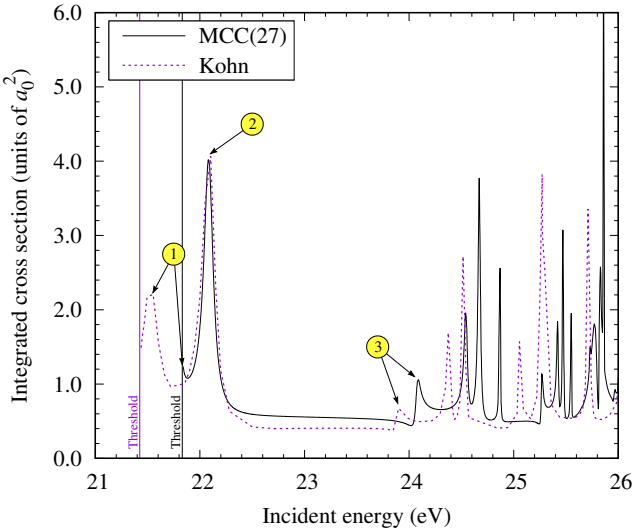

FIG. 7. Resonances in the fixed-nuclei $X\,^1\Sigma^+ \rightarrow a\,^3\Sigma^+$ excitation cross section calculated at the equilibrium internuclear separation ($R = 1.455\ a_0$). Comparison is between the present MCC(27) model and the complex Kohn calculations of Orel et al. [21]. Circled numbers indicate features which are discussed in the text.

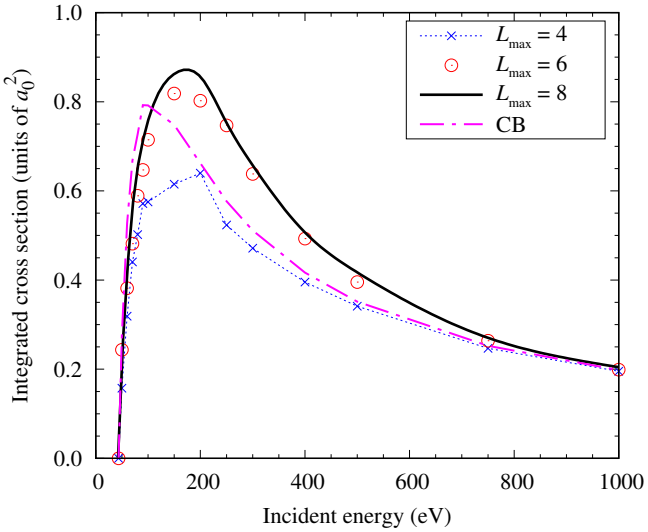

FIG. 8. Convergence studies for ionization of the ground electronic state of HeH^+ at $R = 1.518\ a_0$. Convergence is tested with respect to the size of the projectile partial-wave expansion L_{max} used with the MCCC(546) model.

systematic energy shift is not present for this feature. We have performed test calculations with less accurate target structure and found that the position of feature two is just as sensitive to changes in the target energies as the other features, so it appears that the agreement between the MCCC and Kohn calculations here is a coincidence. Overall, the similar magnitude of the background scattering cross section and appearance of similar resonance structures in the two calculations is a useful verification that the MCCC method has been correctly implemented for HeH^+.

The larger models in Fig. 6 are run on a courser energy grid and hence the apparent numerical instability near threshold is in fact a result of slight changes in resonance energies between the models (e.g. the three MCCC models differ at the first energy point after threshold for the $C\,^1\Pi$ excitation, but are otherwise in perfect agreement). Since the adiabatic-nuclei and fixed-nuclei approximations break down near resonances, the positions and magnitudes of the resonances in these cross sections are not physically significant. A proper study of these resonances would require a different technique, such as the electronic and vibrational close-coupling method of Scarlett et al. [41], the R-matrix approach of Schneider et al. [42, 43], or one of several methods based on Feschbach's projection-operator formalism [44]. In Ref. [41], we showed that for the case of e^--H_2 scattering the true resonances are much smaller than those in the fixed-nuclei cross sections. Taking these facts into consideration, we make no attempt to map out resonances in our converged results. For most transitions the models which neglect the target continuum [MCC(9), MCC(27), and MCC(98)] differ substantially from those which include it, demonstrating the importance of coupling to ionization channels. The MCCC(546) model yields sufficiently converged cross sections over the entire energy range. The rates of convergence for the $n = 3$ excitations are similar, and we find that the MCCC(546) model is appropriate for all transitions of interest. For completeness, convergence studies for the $n = 3$ states are presented in the appendix.

C. Partial-wave convergence

With convergence established with respect to the number of target states included in the close-coupling expansion, we now verify convergence with respect to the projectile partial-wave expansion. The calculations in Sec. III B had $L_{max} = 6$ (with Coulomb-Born completion applied on top of this), and we now repeat the MCCC(546) calculations with $L_{max} = 4$ and 8.

In Fig. 8 we present partial-wave convergence studies for ionization of the $X\,^1\Sigma^+$ state. The $L_{max} = 4$ calculation is clearly not converged, while the $L_{max} = 6$ and 8 calculations are in agreement except for a small ($\approx 5\%$) discrepancy at the cross-section maximum, indicating the that $L_{max} = 8$ model is sufficient. In Fig. 9, partial-wave convergence studies are presented for excitation of the $n = 2$ electronic states. The exchange transitions are clearly converged with $L_{max} = 8$, however for excitation of the singlet states there is still a small discrepancy between the $L_{max} = 6$ and 8 results at the cross-section peak. As with the ionization cross section the difference is only around 5% and we expect the error in the $L_{max} = 8$ cross section compared to a fully-converged result to be smaller than that. Therefore, we conclude that

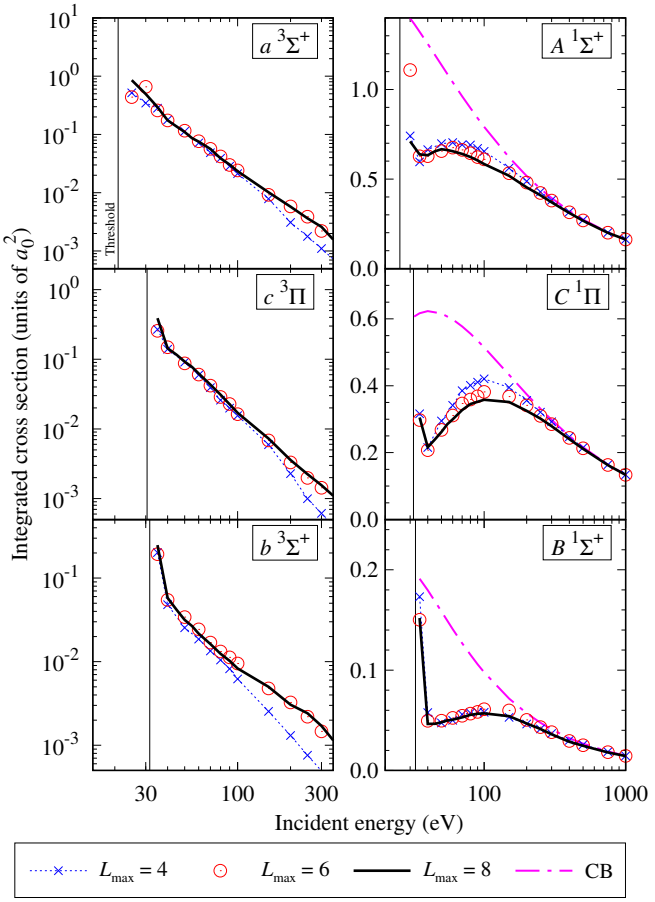

FIG. 9. Convergence studies for excitation of the $n=2$ states from the ground electronic state of HeH^+ at $R = 1.518\ a_0$. Convergence is tested with respect to the size of the projectile partial-wave expansion L_{max} used with the MCCC(546) model. The Coulomb-Born (CB) cross sections are also shown for the singlet states.

the $L_{max} = 8$ model is satisfactory, and will account for an uncertainty of 5% in the final results. We have also found the $L_{max} = 8$ model to yield sufficiently converged cross sections for excitation of the $n=3$ electronic states, as shown in the appendix.

D. Adiabatic-nuclei calculations

Performing AN calculations is much more computationally expensive than in the FN approximation since each energy requires the electronic scattering problem to be solved at a number of different internuclear separations. At present, we have conducted AN calculations using the MCC(27) model at low energies in order to extend the excitation cross sections down to the correct threshold.

AN calculations were performed up to 40 eV using a fine R mesh (steps of 0.01 between 1 and 2) to ensure the accuracy of the integration over R in Eq. (27). This

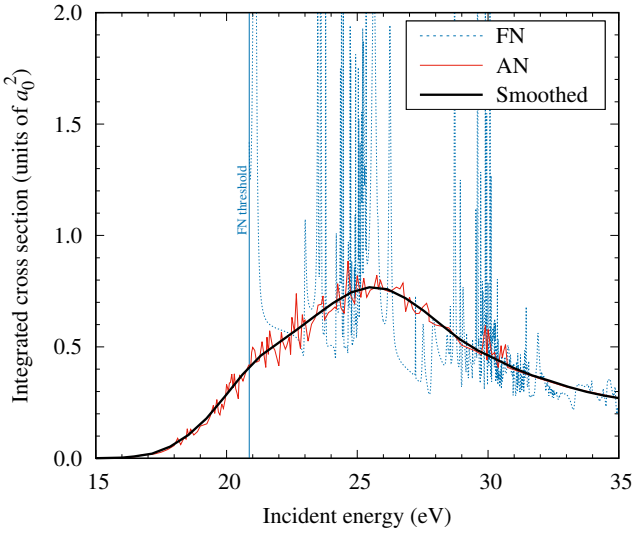

FIG. 10. Calculations of the $X\ ^1\Sigma^+(v=0) \rightarrow a\ ^3\Sigma^+$ cross section using the MCC(27) model. The fixed-nuclei (FN) result shows a large number of resonances, which are diminished in the adiabatic-nuclei (AN) calculations.

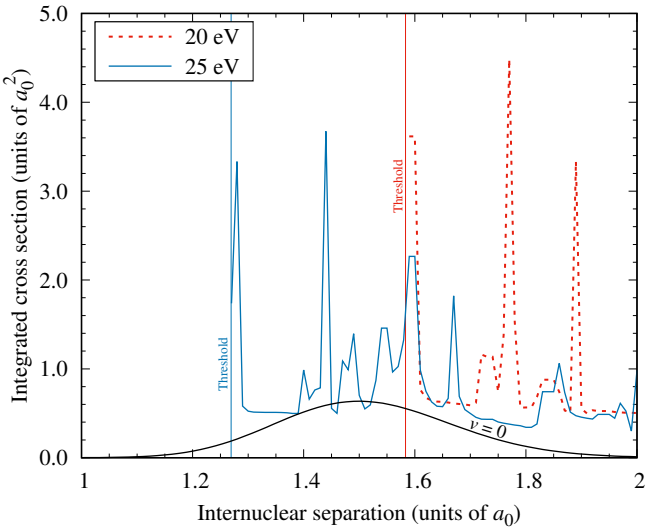

FIG. 11. The MCC(27) $X\ ^1\Sigma^+ \rightarrow a\ ^3\Sigma^+$ cross section at 20 and 25 eV incident energies presented as a function of internuclear separation. Also shown is the square of the $v=0$ vibrational wave function (on an arbitrary scale).

range covers the extent of the $v = 0$ vibrational wave function (see Fig. 3). In Fig. 10 we compare the FN and AN cross sections for the $X\ ^1\Sigma^+ \rightarrow a\ ^3\Sigma^+$ transition in the MCC(27) model, and in Fig. 11 we give examples of the R-dependent cross section at 20 and 25 eV incident energies. There are a large number of resonances in both the FN and R-dependent cross sections, and the AN cross section we have calculated shows that the resonances are reduced in magnitude substantially, but do not disappear altogether. It is likely that the remaining spikes in the AN cross section are numerical artifacts

which would be further reduced by the use of a denser R grid. Since the AN approximation is not accurate near resonances we must accept that the cross section in this region is inherently uncertain, and hence there is little to be gained from attempting to improve on these calculations. Instead, in Fig. 10 we have drawn a smooth cross section which best represents the raw AN calculation without any jagged behavior. The small shoulder in the cross section around 21 eV is likely a result of averaging over the broader shape resonance near the threshold of the fixed-nuclei calculation. It is interesting to note that while the FN cross section is non-zero at threshold, the AN cross section is zero at threshold and rises slowly as the incident energy increases. This behavior is a result of the vibrational dynamics and is characteristic of cross sections for excitation of states with repulsive potential-energy curves (see the same for H_2 in Ref. [45]).

Orel et al. [21] performed FN and AN calculations of the $X\,^1\Sigma^+ \rightarrow a\,^3\Sigma^+$ transition between 21 and 26 eV, and reported similar resonance structures in the FN cross section (as discussed above and shown in Fig 7). However, rather than accounting for the R-dependence of the cross sections (as seen in Fig. 11), Orel et al. [21] took the FN cross section (in their case calculated at an internuclear separation of 1.455), and shifted it to reflect the R dependence of the excitation thresholds:

$$\sigma(E_i, R) \approx \sigma(E_i - \epsilon(R_0) + \epsilon(R), R_0), \qquad (29)$$

where E_i is the incident energy, R_0 is the equilibrium separation, and ϵ is the (R-dependent) vertical excitation energy. This shifted cross section was then used in place of the R-dependent cross section in Eq. (27). The effect of this approach was to produce a cross section representing the smooth background scattering contribution without the presence of resonances. The later complex Kohn calculations of Ertan et al. [24] applied the AN approximation with a proper account of the R dependence of $\sigma(E_i, R)$, and produced cross sections for excitation of the $a\,^3\Sigma^+$ and $A\,^1\Sigma^+$ states up to 40 eV. In Fig. 12 we compare the AN MCC(27) calculations for the $a\,^3\Sigma^+$ and $A\,^1\Sigma^+$ excitations with the two sets of Kohn calculations. Ertan et al. [24] also found resonance structures in their AN cross sections and produced a smooth curve with the resonances removed, which is what we compare with here. The MCC(27) calculation for the $a\,^3\Sigma^+$ state is in agreement with the 1991 calculation of Orel et al. [21] at 20 eV, but is larger at the cross-section peak. Since the two calculations have a similar magnitude of the FN cross section at all energies, the difference here is a result of different ways in which the AN approximation was applied. Although the 2016 Kohn calculations of Ertan et al. [24] apply the AN approximation in the same way that we have, their cross section for the $a\,^3\Sigma^+$ state is much lower than ours at nearly all energies, and also lower than the 1991 Kohn calculations. The FN cross section for this transition in the 2016 calculations (see Fig. 2 of Ref. [24]) is about 30% smaller than what was obtained in the 1991 calculations, which explains the difference. The reason for the discrepancy between the two FN Kohn calculations is unclear, and is not discussed in Ref. [24]. For the $A\,^1\Sigma^+$ excitation, the MCC(27) and 2016 Kohn calculations are in good agreement from 20 to 27 eV, with differences in shape but similar overall magnitude between 27 and 40 eV.

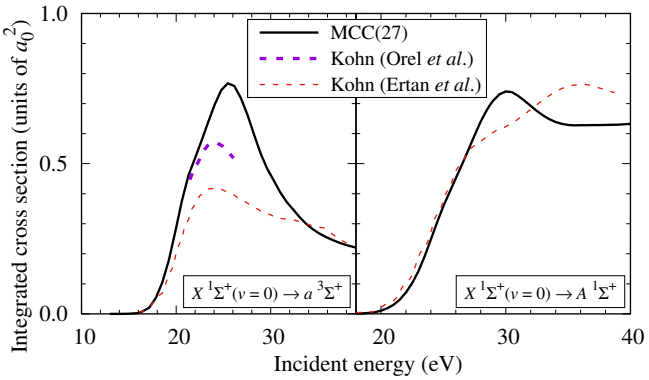

FIG. 12. Comparison of the adiabatic-nuclei MCC(27) calculations with the complex Kohn calculations of Orel et al. [21] and Ertan et al. [24] for excitation of the $a\,^3\Sigma^+$ and $A\,^1\Sigma^+$ states.

IV. RESULTS AND DISCUSSION

In Figs. 13 and 14 we present the MCCC cross sections for excitation of the $n=2$–3 electronic states and ionization of HeH^+ from the $X\,^1\Sigma^+(v=0)$ state. The final results for the discrete excitations have been produced by merging the AN MCC(27) $L_{\max}=6$ and FN MCCC(546) $L_{\max}=8$ models to improve the accuracy at low energies and enforce the correct excitation thresholds. The two models are joined between 30 and 40 eV, depending on the transition, at a point where both MCC(27) and MCCC(546) produce a similar FN cross section. For transitions where the MCC(27) model is not fully converged in this region (several of the $n=3$ excitations) the AN MCC(27) cross section is simply scaled to match the converged MCCC(546) cross section at the matching point. While this is not perfect, it is only a small energy region which is affected, and this approach allows us to produce cross sections for all excitations which smoothly approach the correct threshold. As mentioned in Sec. III D, although this is a charged target the AN cross sections for these dissociative transitions are all zero at threshold, due to the vibrational dynamics. The ionization cross section is less accurate near threshold since it is obtained only from the FN calculation, but with convergence now established in the FN cross section it will be possible to perform larger-scale AN calculations in the future should the need arise. This would also allow the study of scattering on excited vibrational levels, as we have done recently for the e^--H_2 system [15, 16].

In Fig. 15 we present a selection of differential cross

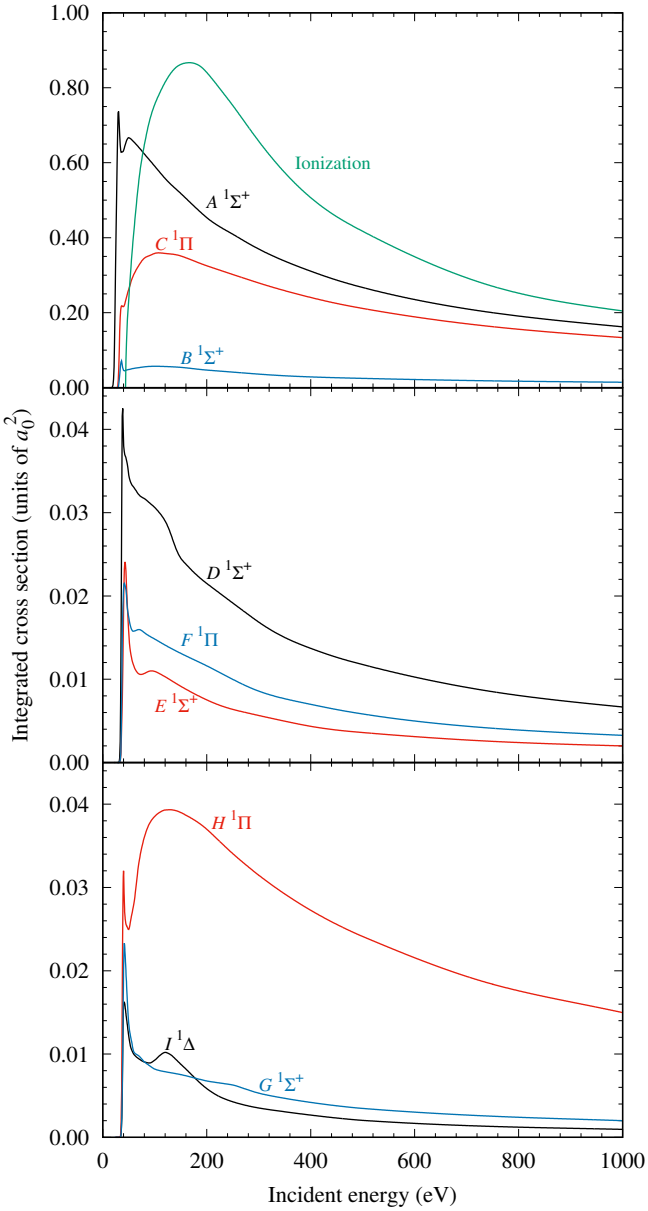

FIG. 13. Electron-impact cross sections for excitation of the $n=2$–3 singlet states, and ionization of HeH^+.

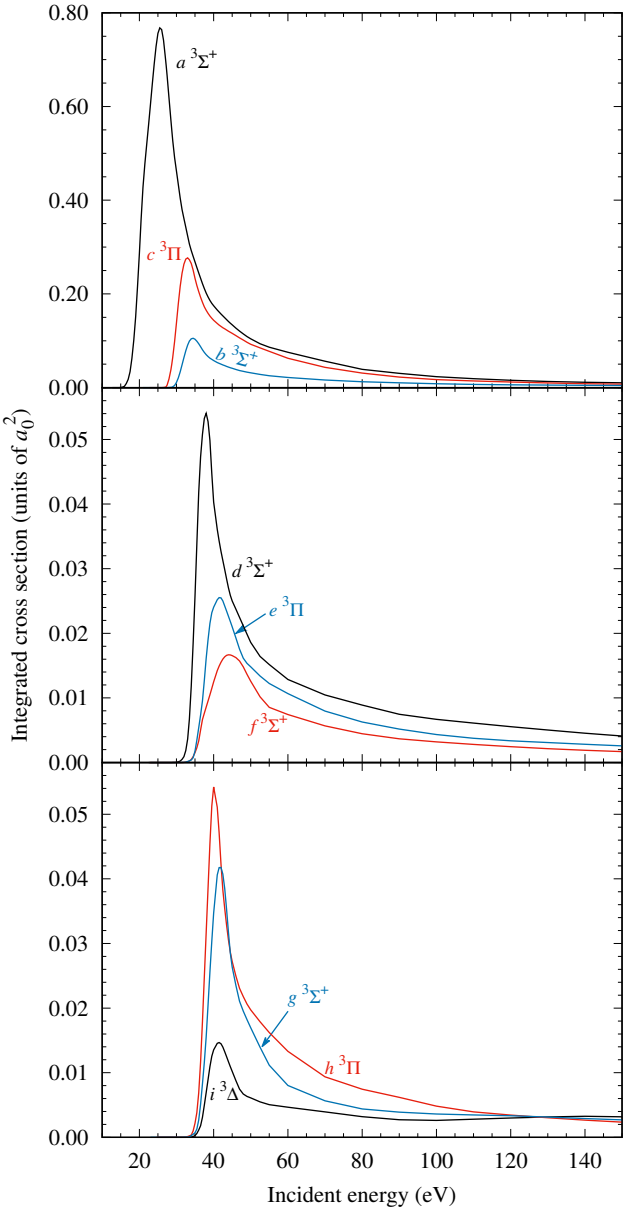

FIG. 14. Electron-impact cross sections for excitation of the $n=2$–3 triplet states of HeH^+.

sections (DCS), for excitation of the $n=2$ states at five different incident energies between 30 and 90 eV. No previous calculations or measurements of DCS exist for this system. If required, DCS for additional transitions or incident energies can be calculated and made available upon request.

There are very few measurements available for comparison, and aside from the calculations of the $a\,^3\Sigma^+$ excitation from Orel et al. [21] and the $a\,^3\Sigma^+$ and $A\,^1\Sigma^+$ excitations from Ertan et al. [24], there are no previous calculations of electronic excitation or ionization of HeH^+ (that we are aware of). Lecointre et al. [32] and Strömholm et al. [31] have both measured cross sections for electron-impact dissociation of HeH^+ leading to He^+ fragments, and hence we now utilize the calculated cross sections to estimate the cross section for He^+ production. Referring to Table I, the electronic states under present investigation which produce He^+ fragments upon dissociation are $a\,^3\Sigma^+$, $A\,^1\Sigma^+$, $D\,^1\Sigma^+$, $f\,^3\Sigma^+$, $E\,^1\Sigma^+$, $e\,^3\Pi$, and $g\,^3\Sigma^+$. Additionally, the ground electronic state of HeH^{2+} is repulsive and produces He^+ fragments. Since all electronic excitations and ionization from the $X\,^1\Sigma^+(v=0)$ state lead to dissociation (see Fig. 1), the dissociation cross section for particular atomic fragments is obtained simply by summing the cross sections for the relevant transitions. Lecointre et al. [32] also measured He^{2+} fragment resulting from the ionization-with-excitation process producing HeH^{2+} in its first electronically-excited state, however

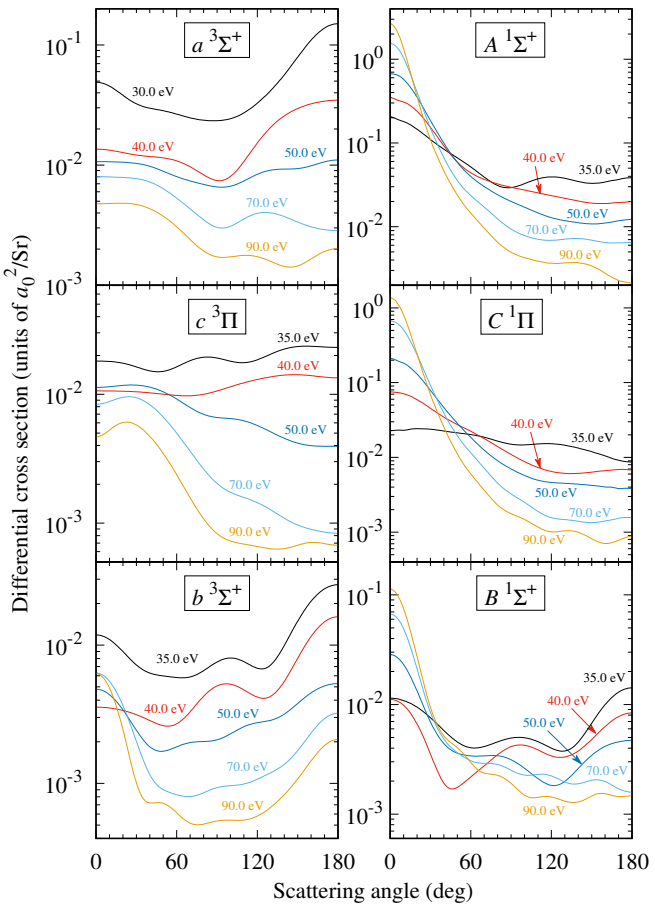

FIG. 15. Differential cross sections for electron-impact excitation of the $n=2$ states of HeH^+ at a selection of incident energies.

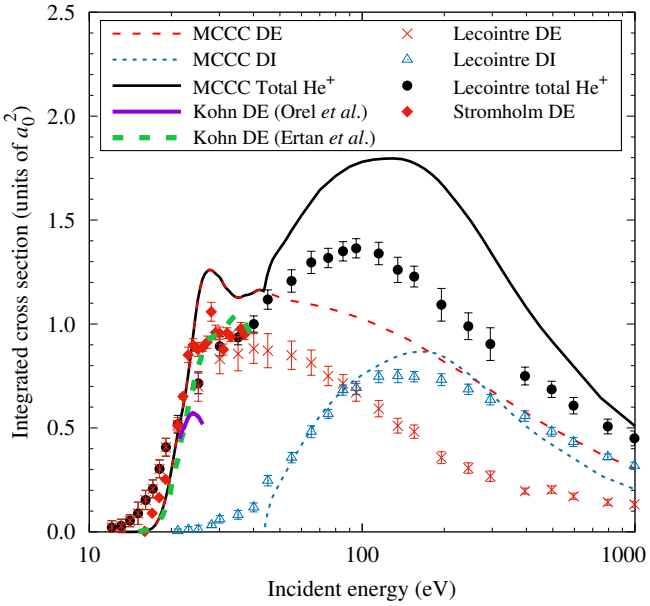

FIG. 16. Cross sections for production of He^+ from electron-impact dissociative excitation (DE) and ionization (DI) of HeH^+. Comparison is made between the MCCC calculations, the complex Kohn calculations of Orel et al. [21] and Ertan et al. [24], and the measurements of Lecointre et al. [32] and Strömholm et al. [31].

their cross section for this process is two orders of magnitude smaller than it is for ionization producing He^+ and can be neglected.

In Fig. 16 we present our estimates for dissociative excitation (DE) and ionization (DI) leading to He^+ fragments, as well as the total He^+ production cross section (DE + DI). The threshold in the measurements of Lecointre et al. [32] is lower than the first electronically-inelastic threshold due to the contribution from resonance-enhanced dissociation through the $X\,^1\Sigma^+$ vibrational continuum, a process which has been studied by Orel and Kulander [23]. Strömholm et al. [31] presented their measurements of the direct and indirect processes separately, and it is only the former which we present in the figure. The first three experimental points of Strömholm et al. [31] above threshold are somewhat larger than the MCCC calculation, then between 20 and 24 eV there is good agreement between the two, and at the peak of the DE cross section the MCCC calculation is about 20% larger than the highest experimental point. The 1991 Kohn calculations are considerably lower than the Strömholm et al. [31] measurements and somewhat lower than the measurements of Lecointre et al. [32]. Although the 2016 Kohn calculation for the $a\,^3\Sigma^+$ state is lower than the 1991 Kohn cross section (see Fig. 12), their inclusion of the $A\,^1\Sigma^+$ state increases the DE cross section to be in better agreement with the measurements. Since there is reasonable agreement between the MCCC calculations and the 2016 Kohn calculations for the $a\,^3\Sigma^+$ and $A\,^1\Sigma^+$ states at 40 eV, the slightly higher DE cross section obtained in the present work for this energy is due to our inclusion of higher electronic states. However, the much larger discrepancy around 25 eV is due entirely to the much smaller $a\,^3\Sigma^+$ cross section obtained by Ertan et al. [24]. Given the discrepancy between the two experiments around 25 eV, and the unsatisfactory agreement between the three calculations, there is insufficient information to draw any meaningful conclusions here other than more experimental and theoretical investigation would be most welcome.

From the peak of the DE cross section to high energies the MCCC calculation is systematically larger than the measured DE cross section of Lecointre et al. [32]. It is worth noting that the ion source used in the experiment of Ref. [32] produced HeH^+ in various vibrational levels, with populations ranging from 0.52 for $v=0$ to 0.01 for $v \geq 5$. However, we have shown previously [9, 10, 46] that cross sections for dissociation of vibrationally-excited H_2 and H_2^+ are larger than for scattering on the ground vibrational level, and if the same is true for HeH^+ then the presence of excited vibrational states cannot explain the present discrepancy between theory and experiment. This of course should be explored further in future work.

The agreement between MCCC and experiment is better for DI, though there is still some deviation at the peak and at high energies. The MCCC DI cross section is not correct at near-threshold energies since it is calculated in the FN approximation, but this does not account for the much lower threshold in the measured ionization cross sections. It can, however, be explained by the presence of vibrationally-excited ions in the experiment since their ionization energy is smaller. Due to the discrepancy between the measured and calculated DE cross sections, the total MCCC He^+ production cross section (sum of DE and DI) is larger than the results of Lecointre et al. [32], with the difference being as large as 30% at the cross-section maximum.

In Fig. 17 we present the cross sections for production of He^+ and H^+ ions. Referring again to Table I, the cross section for production of H^+ via DE is obtained by summing cross sections for excitation of the $c\,^3\Pi$, $b\,^3\Sigma^+$, $B\,^1\Sigma^+$, $d\,^3\Sigma^+$, $F\,^1\Pi$, $i\,^3\Delta$, $I\,^1\Delta$ $h\,^3\Pi$, $H\,^1\Pi$, and $G\,^1\Sigma^+$ states (we expect the contribution from direct dissociation of the $X\,^1\Sigma^+$ continuum to be negligible). The DI process leads to production of both He^+ and H^+ ions.

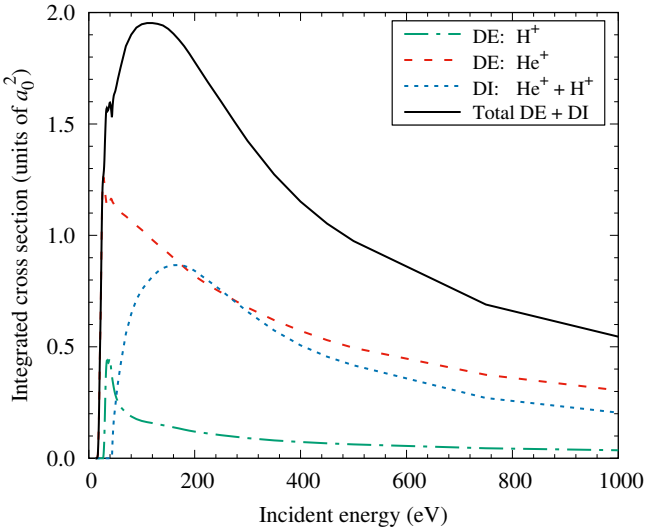

FIG. 17. Cross sections for production of He^+ and H^+ from electron-impact dissociation of HeH^+, as well as total dissociation (sum of He^+ and H^+ production).

V. CONCLUSIONS

We have presented calculations of 10–1000 eV electron scattering on the $X\,^1\Sigma^+(v=0)$ state of HeH^+ using the molecular convergent close-coupling (MCCC) method. Cross sections were calculated for ionization, as well as excitation of the $a\,^3\Sigma^+$, $A\,^1\Sigma^+$, $c\,^3\Pi$, $b\,^3\Sigma^+$, $C\,^1\Pi$, $B\,^1\Sigma^+$, $d\,^3\Sigma^+$, $D\,^1\Sigma^+$, $f\,^3\Sigma^+$, $E\,^1\Sigma^+$, $e\,^3\Pi$, $F\,^1\Pi$, $i\,^3\Delta$, $I\,^1\Delta$, $h\,^3\Pi$, $H\,^1\Pi$, $g\,^3\Sigma^+$, and $G\,^1\Sigma^+$ electronic states, representing all states which converge to the $n=2$ and 3 states of Li^+ in the united-atoms limit.

Detailed convergence studies were performed, with the largest calculation having 549 electronic states in the close-coupling expansion and a maximum projectile partial-wave angular momentum of 8. Higher partial waves were accounted for using the Coulomb-Born approximation to ensure the calculated cross sections are accurate over the entire incident energy range. Convergence was verified within 5% with respect to both the number of target states and projectile partial waves included in the close-coupling expansion. Together, we estimate an uncertainty of 10% in the calculated cross sections. The MCCC target excitation energies are accurate to within 1%, as verified by comparison with the calculations of Jungen and Jungen [34].

Calculations were performed in the fixed-nuclei approximation, however the adiabatic-nuclei approximation was applied to the excitation cross sections at low energies where the fixed-nuclei approximation breaks down. Although the fixed-nuclei excitation cross sections are non-zero at the fixed-nuclei threshold, as is characteristic of charged targets, the adiabatic-nuclei cross sections all approach zero at threshold due to the effects of vibrational motion. We found that the relative contribution of exchange scattering to the ionization cross section is much larger for HeH^+ than for the corresponding atomic system (e^--Li^+), and must be included for incident energies up to 20 times the ionization threshold. Consequently, the Coulomb-Born approximation does not become valid for ionization of HeH^+ until 1000 eV.

Cross sections for H^+ and He^+ ion production following dissociative excitation and ionization were also produced, and comparison with measurements of the latter by Lecointre et al. [32] showed a discrepancy of up to 30% between theory and experiment. Further theoretical and experimental investigation is required to understand the source of the disagreement and produce recommended cross sections.

With convergence now established in the ionization and $n=2$–3 excitation cross sections in the fixed-nuclei approximation, future work can be directed towards studies of scattering on vibrationally excited HeH^+ and its isotopologues using the adiabatic-nuclei approximation. This would also allow kinetic-energy-release distributions to be calculated for the atomic fragments following dissociation, as we have done previously for H_2^+ [47].

The results presented here can be downloaded from the MCCC database [48].

Appendix: ADDITIONAL CONVERGENCE STUDIES

Convergence studies for excitation of the $n=3$ electronic states of HeH^+ are presented in Figs. 18 and 19. Refer to Secs. III B and III C for discussion. Note that the MCC(9) model does not contain the $n=3$ states so it is not included here.

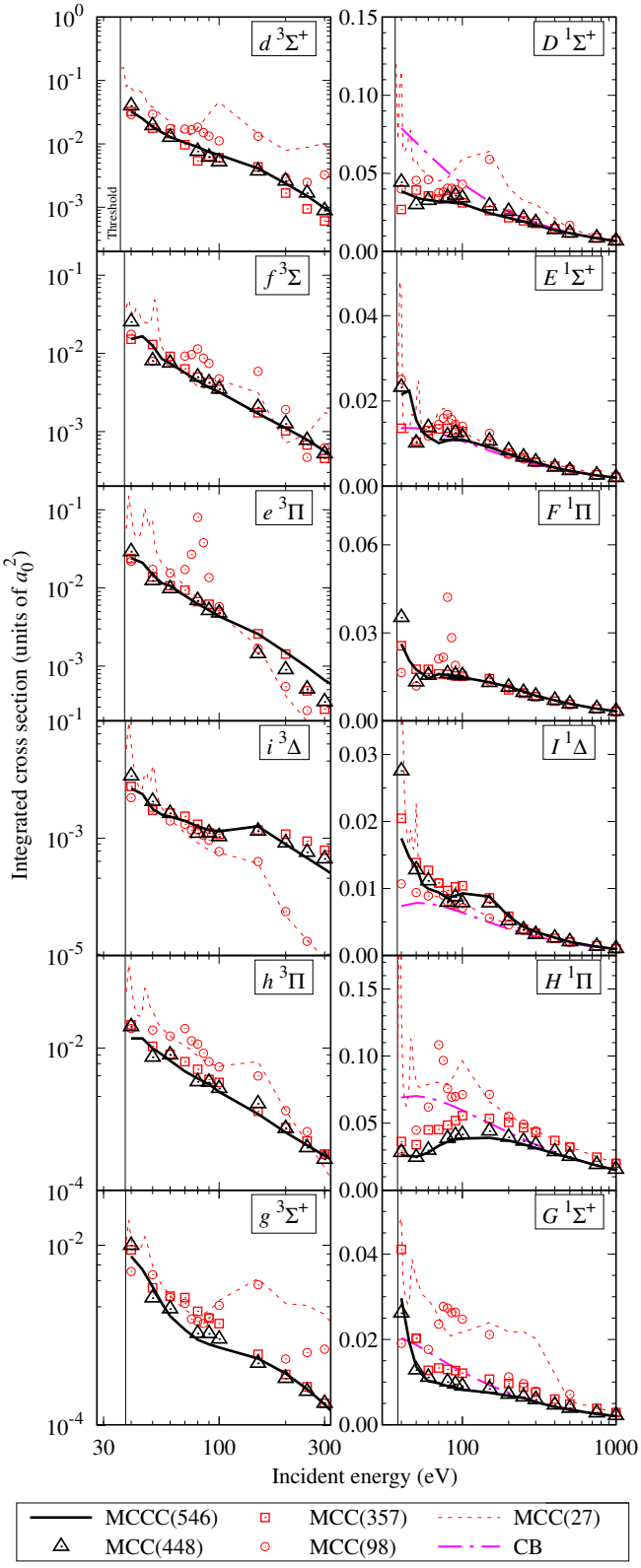

FIG. 18. Convergence studies for excitation of the $n=3$ electronic states from the $X\,^1\Sigma^+$ state of HeH^+ at $R=1.518$ a_0. Convergence is tested with respect to the number of target states included in the close-coupling expansion. The Coulomb-Born (CB) cross sections are also shown for the singlet states. Refer to Sec. III B for discussion.

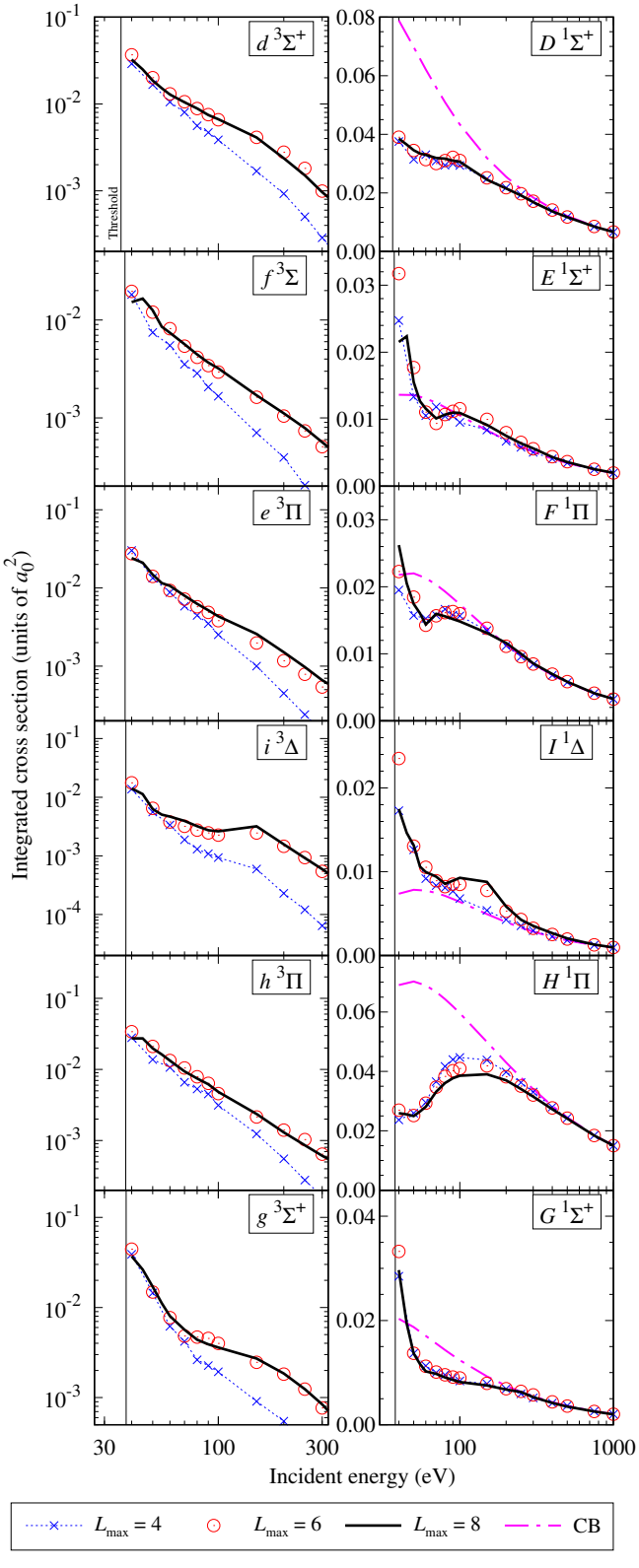

FIG. 19. Convergence studies for excitation of the $n=3$ states from the ground electronic state of HeH^+ at $R=1.518$ a_0. Convergence is tested with respect to the size of the projectile partial-wave expansion L_{max} used with the MCCC(546) model. The Coulomb-Born (CB) cross sections are also shown for the singlet states. Refer to Sec. III C for discussion.

ACKNOWLEDGMENTS

We are grateful to Jérôme Loreau for supplying data in electronic form, and Marco Padovani and Ann Orel for useful discussions. This research was supported by the Australian Government through the Australian Research Council's *Discovery Projects* funding scheme (project DP190101195), and by the United States Air Force Office of Scientific Research. The authors acknowledge the Texas Advanced Computing Center (TACC) at The University of Texas at Austin for providing HPC resources that have contributed to the research results reported within this paper. We also acknowledge the support of the Australasian Leadership Computing Grants scheme, with computational resources provided by NCI Australia, an NCRIS enabled capability supported by the Australian Government. Additional HPC resources were provided by the Pawsey Supercomputing Research Centre with funding from the Australian Government and the Government of Western Australia. M.C.Z would like to specifically acknowledge the support of the Los Alamos National Laboratory (LANL) Laboratory Directed Research and Development program project number 20200356ER. LANL is operated by Triad National Security, LLC, for the National Nuclear Security Administration of the U.S. Department of Energy under Contract No. 89233218NCA000001.

[1] G. Theodorakopoulos, S. C. Farantos, R. J. Buenker, and S. D. Peyerimhoff, J. Phys. B At. Mol. Phys. **17**, 1453 (1984).
[2] J. Loreau, J. Liévin, P. Palmeri, P. Quinet, and N. Vaeck, J. Phys. B At. Mol. Opt. Phys. **43**, 065101 (2010).
[3] H. Takagi, Fusion Sci. Technol. **63**, 406 (2013).
[4] J.-S. Yoon and M.-Y. Song, *Data evaluation of helium and its isotopes for fusion plasma (INDC(NDS)–0728)* (2017), URL https://inis.iaea.org/search/search.aspx?orig_q=RN:49066520.
[5] S. Lepp, P. C. Stancil, and A. Dalgarno, J. Phys. B At. Mol. Opt. Phys. **35**, 393 (2002).
[6] S. Bovino, M. Tacconi, F. A. Gianturco, and D. Galli, Astron. Astrophys. **529**, 1 (2011).
[7] W. Roberge and A. Dalgarno, Astrophys. J. **255**, 489 (1982).
[8] M. C. Zammit, D. V. Fursa, J. S. Savage, and I. Bray, J. Phys. B At. Mol. Opt. Phys. **50**, 123001 (2017).
[9] M. C. Zammit, D. V. Fursa, and I. Bray, Phys. Rev. A **88**, 062709 (2013).
[10] M. C. Zammit, D. V. Fursa, and I. Bray, Phys. Rev. A **90**, 022711 (2014).
[11] M. C. Zammit, J. S. Savage, D. V. Fursa, and I. Bray, Phys. Rev. Lett. **116**, 233201 (2016).
[12] M. C. Zammit, J. S. Savage, D. V. Fursa, and I. Bray, Phys. Rev. A **95**, 022708 (2017).
[13] M. C. Zammit, D. V. Fursa, J. S. Savage, L. Chiari, A. Zecca, and M. J. Brunger, Phys. Rev. **95**, 022707 (2017).
[14] L. H. Scarlett, J. S. Savage, D. V. Fursa, I. Bray, M. C. Zammit, and B. I. Schneider, Phys. Rev. A **103**, 032802 (2021).
[15] L. H. Scarlett, D. V. Fursa, M. C. Zammit, I. Bray, Yu. Ralchenko, and K. D. Davie, At. Data Nucl. Data Tables **137**, 101361 (2021).
[16] L. H. Scarlett, D. V. Fursa, M. C. Zammit, I. Bray, Yu. Ralchenko, and K. D. Davie, At. Data Nucl. Data Tables **139**, 101403 (2021).
[17] L. H. Scarlett, D. K. Boyle, M. C. Zammit, Y. Ralchenko, I. Bray, and D. V. Fursa, At. Data Nucl. Data Tables **in press**, 101534 (2022).
[18] D. Wünderlich, L. H. Scarlett, S. Briefi, U. Fantz, M. C. Zammit, D. V. Fursa, and I. Bray, J. Phys. D. Appl. Phys. **54**, 115201 (2021).
[19] M. Padovani, S. Bialy, D. Galli, A. V. Ivlev, T. Grassi, L. H. Scarlett, U. S. Rehill, M. C. Zammit, D. V. Fursa, and I. Bray, Astron. Astrophys. **658**, A189 (2022).
[20] K. Verhaegh, B. Lipschultz, J. R. Harrison, B. P. Duval, A. Fil, M. Wensing, C. Bowman, D. S. Gahle, A. Kukushkin, D. Moulton, et al., Nucl. Fusion **61** (2021).
[21] A. E. Orel, T. N. Rescigno, and B. H. Lengsfield, Phys. Rev. A **44**, 4328 (1991).
[22] A. E. Orel, K. C. Kulander, and T. N. Rescigno, Phys. Rev. Lett. **74**, 4807 (1995).
[23] A. E. Orel and K. C. Kulander, Phys. Rev. A - At. Mol. Opt. Phys. **54**, 4992 (1996).
[24] E. Ertan, A. Larson, and A. E. Orel, EPJ Web Conf. **113**, 4 (2016).
[25] Å. Larson and A. E. Orel, Phys. Rev. A **59**, 3601 (1999).
[26] R. Čurík, D. Hvizdoš, and C. H. Greene, Phys. Rev. Lett. **124**, 043401 (2020).
[27] J. R. Hamilton, A. Faure, and J. Tennyson, Mon. Not. R. Astron. Soc. **455**, 3281 (2016).
[28] M. Ayouz and V. Kokoouline, Atoms **4**, 30 (2016).
[29] M. Khamesian, M. Ayouz, J. Singh, and V. Kokoouline, Atoms **6**, 1 (2018).
[30] M. Ayouz and V. Kokoouline, Atoms **7**, 67 (2019).
[31] C. Strömholm, J. Semaniak, S. Rosén, H. Danared, S. Datz, W. van der Zande, and M. Larsson, Phys. Rev. A **54**, 3086 (1996).
[32] J. Lecointre, J. J. Jureta, X. Urbain, and P. Defrance, J. Phys. B At. Mol. Opt. Phys. **47**, 015203 (2014).
[33] H. H. Michels, J. Chem. Phys. **44**, 3834 (1965).
[34] M. Jungen and C. Jungen, Mol. Phys. **113**, 2333 (2015).
[35] I. Bray, Phys. Rev. A **49**, 1066 (1994).
[36] L. H. Scarlett, J. S. Savage, D. V. Fursa, I. Bray, and M. C. Zammit, Eur. Phys. J. D **74**, 36 (2020).

[37] W. C. Tung, M. Pavanello, and L. Adamowicz, J. Chem. Phys. **137** (2012).
[38] D. M. Bishop and L. M. Cheung, J. Chem. Phys. **76**, 2492 (1982).
[39] D. V. Fursa and I. Bray, J. Phys. B At. Mol. Opt. Phys. **30**, 5895 (1997).
[40] I. Bray, D. V. Fursa, A. S. Kadyrov, A. Müller, A. Borovik, and S. Schippers, Phys. Rev. A **100**, 012707 (2019).
[41] L. H. Scarlett, I. Bray, and D. V. Fursa, Phys. Rev. Lett. **127**, 223401 (2021).
[42] B. I. Schneider, M. Ledourneuf, and P. G. Burke, J. Phys. B At. Mol. Phys. **12**, L365 (1979).
[43] B. I. Schneider, M. Le Dourneuf, and V. K. Lan, Phys. Rev. Lett. **43**, 1926 (1979).
[44] W. Domcke, Phys. Rep. **208**, 97 (1991).
[45] L. H. Scarlett, D. V. Fursa, J. Knol, M. C. Zammit, and I. Bray, Phys. Rev. A **103**, L020801 (2021).
[46] L. H. Scarlett, J. S. Savage, D. V. Fursa, M. C. Zammit, and I. Bray, Atoms **7**, 75 (2019).
[47] L. H. Scarlett, M. C. Zammit, D. V. Fursa, and I. Bray, Phys. Rev. A **96**, 022706 (2017).
[48] mccc-db.org.